Journal of Materials Chemistry A

Accepted Manuscript

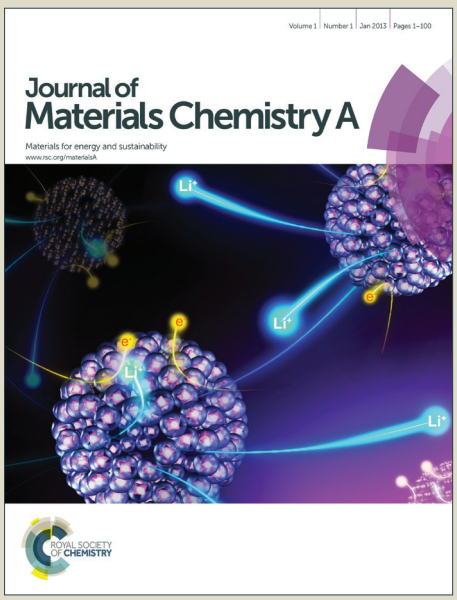

ROYAL SOCIETY OF CHEMISTRY

www.rsc.org/materialsA

Journal of Materials Chemistry A

Dynamic Article Links ►

Cite this: DOI: 10.1039/c0xx00000x

www.rsc.org/xxxxxx

PAPER

Simple one-step synthesis of fluorine-doped carbon nanoparticles as potential alternative metal-free electrocatalysts for oxygen reduction reaction

Gasidit Panomsuwan*[a], Nagahiro Saito[bcd] and Takahiro Ishizaki*[ad]

Received (in XXX, XXX) Xth XXXXXXXXX 20XX, Accepted Xth XXXXXXXXX 20XX
DOI: 10.1039/b000000x

Fluorine-doped carbon nanoparticles (FCNPs) were synthesized *via* a simple one-step solution plasma process for the first time. This synthetic strategy can be achieved at relatively low temperature and atmospheric pressure without the involvement of a metal catalyst. A mixture of toluene ($C_6H_5CH_3$) and trifluorotoluene ($C_6H_5CF_3$) was used as a precursor for the synthesis. Fluorine doping content can be varied from 0.95 to 4.52 at%, depending on the precursor mixing ratio. The structural analyses reveal that FCNPs mainly exhibit a disordered amorphous structure. The incorporation of fluorine atoms results in the creation of more defect sites and disordered structure in the carbon particles. The electrocatalytic activity toward the oxygen reduction reaction (ORR) of FCNPs in an alkaline solution shows a significant improvement with increasing fluorine doping content, as reflected in an increased limiting current density and a positively shifted onset potential. In association with X-ray photoelectron spectroscopy (XPS) analysis, an improved ORR activity is possibly attributed to the intercalation of ionic C–F and semi-ionic C–F bonds in the carbon structure. In addition, FCNPs possess excellent long-term operation durability and strong tolerance to methanol oxidation compared to those of a commercial Pt-based catalyst. Our results in this study not only confirm the applicability of solution plasma process to the synthesis of FCNPs with controllable fluorine doping level but also provide detailed information of FCNPs as potential alternative ORR catalysts for the electrocatalysis research.

1. Introduction

Metal-free heteroatom-doped carbons have attracted enormous interest as promising materials for a fuel cell cathode with the expectation to replace Pt-based carbon catalysts in near future due to their good electrocatalytic activity toward oxygen reduction reaction (ORR), cost effectiveness, long-term cycling stability, and excellent tolerance to methanol and carbon monoxide (CO) oxidations.[1–3] Several theoretical studies have also proven that the disturbance in atomic charge density and spin density distributions by substituting heteroatom into the graphitic carbon frameworks plays a key role in tailoring the electronic arrangement as well as enhancing ORR activity.[4–6] Although there have been many research efforts on metal-free heteroatom-doped carbons in recent years, most of them have focused on the carbon nanomaterials doped with nitrogen,[7–9] boron,[10,11] phosphorus,[12,13] sulfur,[14,15] and their dual or multiple dopants.[16–19] To pave a new way for development in this interesting field, searching a new class of heteroatom-doped carbons beyond nitrogen, boron, sulfur, and phosphorus dopants is a next-step challenge facing researchers. Very recently, Sun *et al* first reported that doping fluorine atoms into sp^2-hybridized carbon framework could effectively enhance the electrocatalytic activity for the ORR in both alkaline and acidic electrolytes.[20–22] This interesting finding has shed new light on the possible use of fluorine-doped carbon materials as a potential alternative ORR catalyst for fuel cells and related applications.

So far, a number of strategies, such as chemical vapor deposition, arc plasma, ball milling, hydrothermal carbonization, and post-thermal treatment, have been proposed and developed to synthesize heteroatom-doped carbons (see Ref. 23–25 and references therein). However, these strategies typically require the introduction of inert gas, high processing temperature, addition of metal catalysts, and multistage synthetic procedures, which consequently hinder the realization of practical applications. Therefore, the development of a simple, low-temperature, and catalyst-free strategy for heteroatom-doped carbons is highly desirable and still remains a challenge. For instance, Feng *et al* demonstrated the synthesis of nitrogen-doped graphene at low temperature (320 °C) using a denotation process with a gram scale yield.[26] Zhang *et al* reported a successful synthesis of nitrogen-doped graphene, from a graphitic carbon template and nitrogen-containing molecules, by a wet chemical synthesis at temperatures as low as 180 °C without high-temperature treatment.[27] Over the past few years, plasma has emerged as a key technology to potentially enable the preparation of heteroatom-doped carbons at relatively low processing temperatures and atmospheric pressure.[28–32] In our previous works, we demonstrated the successful direct synthesis of *in situ* nitrogen-doped carbon nanoparticles *via* a liquid-phase plasma, named solution plasma process, from nitrogen-containing liquid

organic compounds.[33,34] By using this strategy, carbon materials doped with other heteroatoms can also be synthesized simply by selecting an appropriate organic precursor containing the desired heteroatom dopant.[35,36]

In this study, we present for the first time the synthesis of fluorine-doped carbon nanoparticles (FCNPs) with controllable fluorine doping content *via* a solution plasma process. The synthesis can be achieved in a one-step process at room temperature and atmospheric pressure without the addition of metal catalysts. The mixture of toluene and trifluorotoluene (fluorine source) was used as precursor for the synthesis. The effect of fluorine doping content on the morphological, structural, and chemical properties of FCNPs was investigated concurrently and discussed in detail. Moreover, the evolution of electrocatalytic activity for the ORR of FCNPs in an alkaline solution was studied through the role of the fluorine bonding state.

2. Experimental section

2.1 Chemicals

Toluene ($C_6H_5CH_3$, purity 99.5%), ethanol (C_2H_5OH, purity 99.5%), methanol (CH_3OH, purity 99.8%), and 0.1 M potassium hydroxide (KOH) aqueous solution were purchased from Kanto Chemical Co., Inc. Trifluorotoluene ($C_6H_5CF_3$, purity > 98.0%) was purchased from Tokyo Chemical Industry. Nafion® DE 521 solution (5 wt% in mixture of lower aliphatic alcohols and water) and 20 wt% Pt loading on Vulcan XC-72 (20% Pt/C) were purchased from Sigma-Aldrich. All reagents were of analytical grade and used without further purification. Ultrapure water (18.2 MΩ·cm) was obtained from a RFD250NB Aquarius water purification system.

2.2 Synthesis of fluorine-doped carbon nanoparticles

Figure 1 depicts a schematic illustration of solution plasma system used to synthesize FCNPs in this study. A mixture of toluene and trifluorotoluene was varied at the volume ratios of 100:0, 75:25, 50:50, 25:75, and 0:100 with a total volume of 100 mL to adjust the fluorine doping content. A pair of 1 mm-diameter tungsten wire (Nilaco Corporation, purity 99.9%) shielded with an insulating ceramic tube was used as the electrodes and placed at the center of a glass reactor with a gap distance of 1.0 mm. A high bipolar-pulse voltage (~1.0 kV) was applied to the tungsten electrodes using a MPP-HV04 Pekuris bipolar pulse generator (Kurita Seisakusho Co., Ltd.). The pulse duration and repetition frequency were fixed at 0.60 μs and 20 kHz, respectively. Plasma was generated and stably maintained in 100 mL of the mixed precursors under vigorous stirring for 20 min. The carbon particles were produced directly from the plasma zone through the decomposition and recombination processes. During the growth and formation of carbon particles, highly reactive fluorine atoms and radicals interacted with carbon species (*i.e.*, C_2 radicals), leading to the formation of fluorine-doped carbon particles. The detailed formation mechanism of fluorine-doped carbon particles by a solution plasma process can be explained with the manner similar to that described in our previous reports.[33,34] The temperature of precursors after synthesis increased slightly to approximately 30–35 °C, which may suggest the generation of non-thermal plasma. The carbon samples were separated from the liquid precursor by being poured through filter paper, and the filtrated carbon samples were repeatedly washed with ethanol to remove soluble organic compounds until the wash solvent was colorless. The carbon samples were dried at 60 °C in air for 12 h and subsequently ground with an agate mortar and pestle for the further characterizations. The carbons synthesized from the mixtures of toluene and trifluorotoluene at the volume ratios of 100:0, 75:25, 50:50, 25:75, and 0:100 are hereafter designated as CNP, FCNP-1, FCNP-2, FCNP-3, and FCNP-4, respectively. The production rate of carbon yields (solid carbon) synthesized from the precursors at various mixing ratios is given in Table 1. The production rate significantly increases with an increase in the amount of trifluorotoluene in the mixed precursor, which ranges from 2.2 mg min^{-1} for pure toluene (CNP) to 20.3 mg min^{-1} for pure trifluorotoluene (FCNP-4).

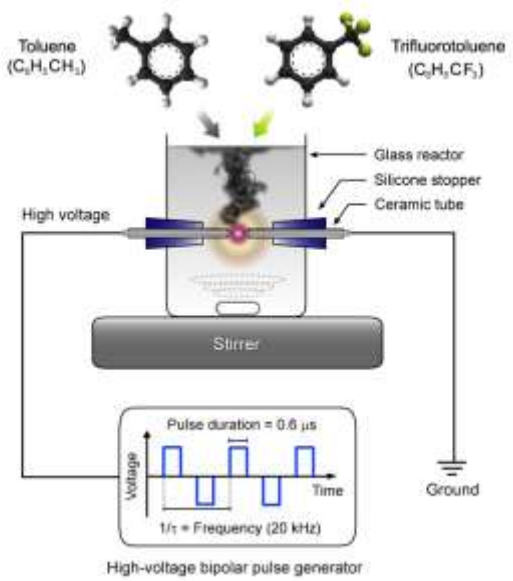

Fig. 1 Schematic illustration of the experimental setup for solution plasma synthesis of fluorine-doped carbon nanoparticles in this study.

2.3 Characterizations

Scanning electron microscopy (SEM) images and energy dispersive spectroscopy (EDS) elemental mapping were acquired on a JEOL JSM-6010LA microscope at an accelerating voltage of 15 kV. Transmission electron microscopy (TEM) images, high-resolution TEM images, and selected area electron diffraction (SAED) patterns were obtained using a JEOL JEM-2100 microscope at an accelerating voltage of 200 kV. Dried carbon samples were dispersed in ethanol under ultrasonication for 15 min. The suspension was then dropped onto a 150 mesh copper TEM grid, and the solvent was allowed to evaporate for 24 h prior to the investigation. Nitrogen adsorption was performed on a Micrometrics Gemini 2375 analyzer equipped with VacPrep 061 at 77 K to investigate the specific surface area. The carbon samples were degassed at 100 °C for 12 h under vacuum before the measurements were taken. The specific surface area was determined using the Brunauer-Emmett-Teller (BET) method in the relative pressure (P/P_0) range of 0.05–0.30. Elemental analysis (EA) was carried out on a Perkin Elmer 2400 Series II CHNS/O analyzer. The phase structure was identified using a Rigaku Ultima IV X-ray diffractometer with monochromatic Cu Kα radiation (λ = 0.154 nm) operating at 40 kV and 40 mA (1.6 kW). Raman spectra were recorded on a JASCO NRS-5100 spectrometer with a laser-excitation wavelength of 532.1 nm. X-ray photoelectron spectroscopy (XPS) measurements were carried out on a JEOL JPS-9010MC spectrometer with monochromatic Mg Kα radiation (1253.6 eV) as an excitation source under ultra high vacuum conditions at a base pressure of 2×10^{-6} Pa. The

emission current and anode voltage were operated at 25 mA and 10 kV, respectively. The binding energy was calibrated using the C 1s peak (284.5 eV). The relevant fitting curves were analyzed using a Gaussian line shape and Shirley background subtraction.

2.4 Electrochemical measurements

A glassy carbon (GC) rotating disk electrode (RDE: 4 mm disk diameter, 0.126 cm^2 disk area) was polished with 0.1 μm diamond slurry followed by 0.05 μm alumina suspension on a polishing pad to obtain the mirror electrode surface. After that, the GC-RDE was ultrasonically cleaned in ultrapure water for 5 min to remove any alumina residues, rinsed with ethanol and ultrapure water, and finally dried with N_2 gas flow. A suspension made with 5.0 mg catalyst, 480 μL ultrapure water, 480 μL ethanol, and 40 μL Nafion aqueous solutions was ultrasonicated until a homogeneous dispersion was obtained. A certain amount of 5 μL of homogeneous suspension (5 mg mL^{-1}) was applied onto a GC-RDE and dried in air for 6 hr at room temperature, resulting in a catalyst loading of approximately 0.2 mg cm^{-2}. Electrochemical measurements were carried out on a computer-controlled ALS-CH model 704ES electrochemical analyzer (CH instrument Inc.) equipped with a rotating ring disk electrode rotator apparatus (RRDE-3A, ALS Co.) and a typical three-electrode system. A platinum coil and Ag/AgCl (saturated KCl) were used as the counter and reference electrodes, respectively. All electrochemical measurements, including cyclic voltammetry (CV), linear sweep voltammetry (LSV), and current–time chronoamperometric response, were evaluated in 0.1 M KOH solution at room temperature. Prior to the measurement, high-purity N_2 or O_2 gases were purged into 0.1 M KOH solutions with a constant flow rate of 50 mL min^{-1} for at least 20 min to ensure the saturation of N_2 or O_2, respectively.

3. Results and discussion

3.1 Morphology

The SEM images of CNP, FCNP-2, and FCNP-4 are displayed in Fig. 2a, 2b, and 2c, respectively. CNP and FCNPs are mainly governed by the agglomeration of carbon particle aggregates, resulting in the formation of three-dimensional (3D) interconnected pore structure. The difference in morphological feature can clearly be observed between CNP and FCNPs, suggesting the change in microstructure and porous structure. To further investigate the morphological and textural properties of the synthesized carbons, the specific surface area of all samples were determined from N_2 adsorption analysis using the BET method. The specific surface area progressively decreases with increasing the fluorine doping content from 236.3 m $^2g^{-1}$ for CNP to 195.6 m $^2g^{-1}$ for FCNP-4 (Table 1). A decrease in specific surface area of FCNPs may possibly be a result of the compact structure and partial collapses of macropores at higher fluorine doping content. The above results suggest that the fluorine doping plays a significant role in altering the morphology and pore structure of the resulting carbon products. Further morphological investigation of CNP and FCNPs was conducted by TEM images, as illustrated in Fig. 2d–f. The carbon particles with a diameter size of 20–40 nm are aggregated with each other, and there is no significant difference in diameter size observed between CNP and FCNPs. The corresponding SAED patterns (the inset of TEM images: Fig. 2d–f) reveal three diffuse rings without any diffraction spots, which implies an amorphous nature of CNP and FCNPs.[37,38] The inner, middle, and outer diffraction rings are associated with (002), (100), and (110) planes, respectively. From high-resolution TEM images (Fig. 2g–i), the presence of short-range orders corresponding to (002) basal plane surrounded by disordered amorphous structure can be observed. Most observed (002) basal planes are quite roughly parallel to each other and bend with interlinking between the planes. The results obtained from both SAED patterns and high-resolution TEM images confirm that CNP and FCNPs synthesized from solution plasma process mainly exhibit a disordered amorphous carbon structure.

3.2 Structural properties

Detailed structural information of CNP and FCNPs was further investigated by XRD and Raman spectroscopy measurements. The XRD pattern of all carbon samples in Fig. 3 reveals a main broad diffraction peak at $2\theta \approx 23°$ and a weaker peak at $2\theta \approx 43°$ corresponding to the (002) and (100)/(101) planes of amorphous carbon, respectively.[39,40] A broad peak characteristic indicates an amorphous structure of CNP and FCNPs, which is in agreement with the aforementioned SAED and HRTEM results. The inset of Fig. 3 shows the enlarged view of XRD patterns around the main 002 diffraction peak of all samples. As the fluorine doping content increases, the intensities of 002 diffraction peak are almost unchanged, while the position of 002 diffraction peak slightly shifts toward a lower 2θ angle. This result implies that the incorporation of fluorine atoms into carbon structure causes the expansion of interplanar spacing (d_{002}). The corresponding d_{002} values of CNP (0.3779 nm) and FCNPs (0.3803–0.3873 nm) are found to be much larger than that of ideal graphite (0.335 nm). The SAED, HRTEM, and XRD results confirm that the CNP and FCNPs are mainly disordered and regarded as amorphous carbon. The Raman spectra of CNP and FCNPs are shown in Fig. 4. Two evident peaks are clearly visible at around 1352–1358 and 1597–1600 cm^{-1}, which are associated with the D-band and G-band, respectively (Table 1). The G-band is related to the E_{2g} phonon of sp^2 bonded carbon atoms, whereas the

Table 1 Production rate, specific surface area (S_{BET}), interlayer spacing (d_{002}), Raman spectroscopy data, bulk elemental composition (obtained from EA), and surface elemental compositions (obtained from XPS) of CNP, FCNP-1, FCNP-2, FCNP-3, and FCNP-4.

	Production rate (mg min^{-1})	S_{BET} (m^2 g^{-1})	d_{002} (nm)	D band (cm^{-1})	G band (cm^{-1})	I_D/I_G	EA (wt%)		XPS (at%)		
							C	H	C	O	F
CNP	2.2	236.3	0.3779	1358	1600	0.85	91.67	1.40	94.58	5.42	-
FCNP-1	3.5	220.8	0.3803	1358	1600	0.86	92.06	1.33	93.86	5.19	0.94
FCNP-2	5.3	221.2	0.3823	1358	1600	0.88	91.81	1.09	92.25	6.03	1.72
FCNP-3	12.3	218.8	0.3819	1356	1599	0.90	90.82	0.90	90.76	5.96	3.28
FCNP-4	20.3	195.6	0.3873	1352	1597	0.94	90.06	0.67	88.68	6.80	4.52

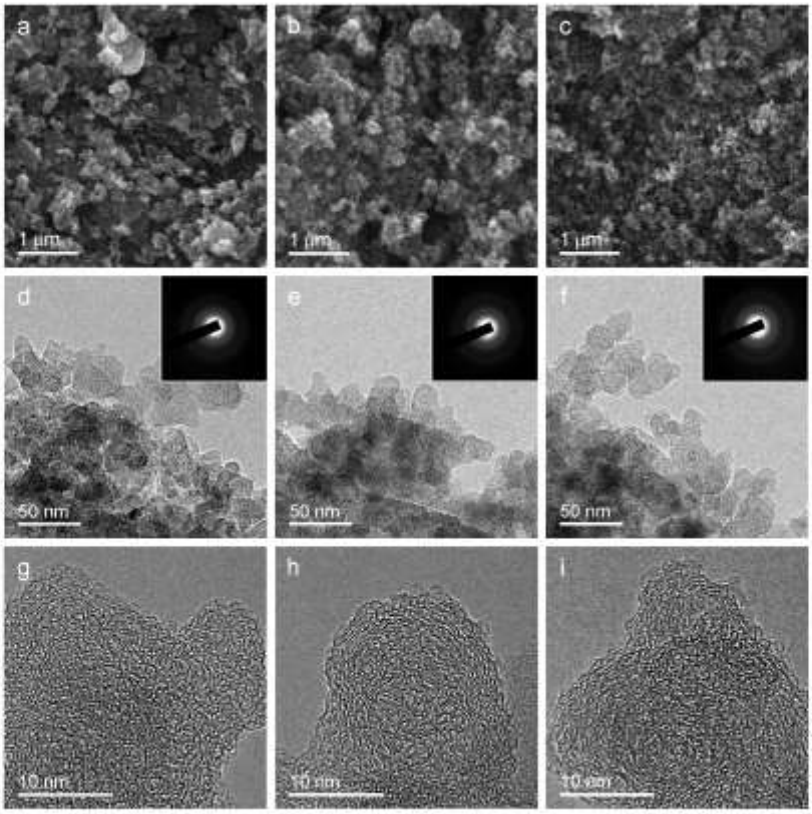

Fig. 2 SEM images of (a) CNP, (b) FCNP-2, and FCNP-4. TEM images of (d) CNP, (e) FCNP-2, and (f) FCNP-4. The inset of each TEM image shows in the corresponding SAED patterns. High-resolution TEM images of (g) CNP, (h) FCNP-2, and (i) FCNP-4.

D-band is attributed to the presence of structural defects and disorder in the carbon lattice.[41,42] It is known that the relative intensity ratio of the D-band to the G-band (I_D/I_G) is typically employed as an indicator to determine the degree of graphitization or defect density in carbon materials.[41,42] The I_D/I_G ratios are estimated to be 0.85, 0.86, 0.88, 0.90, and 0.94 for CNP, FCNP-1, FCNP-2, FCNP-3, and FCNP-4, respectively. An increase in the I_D/I_G ratio with increasing fluorine doping content suggests that the incorporation of fluorine atoms into the carbon structure causes the creation of more structural defect sites and the higher disordered degrees compared to undoped carbon, which is in accordance with the expansion of d_{002} values obtained from the XRD results.

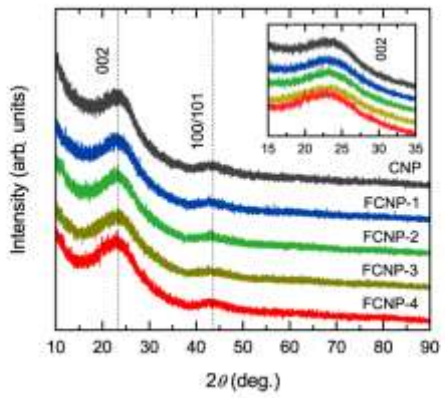

Fig. 3 XRD patterns of CNP, FCNP-1, FCNP-2, FCNP-3, and FCNP-4.The inset shows the enlarged view of the 002 diffraction peak for all samples.

3.3 Elemental composition and chemical bonding state

The content of carbon and hydrogen obtained from elemental analysis (EA) is summarized in Table 1. The hydrogen content decreases with an increase in fluorine doping content from 1.41 to 0.67 wt%. This result implies that the fluorine atoms or ions generated during the synthetic process not only play the role of fluorine doping but also promote the hydrogen abstraction ability, giving rise to the higher production rate. Furthermore, the XPS measurements were carried out to determine the elemental

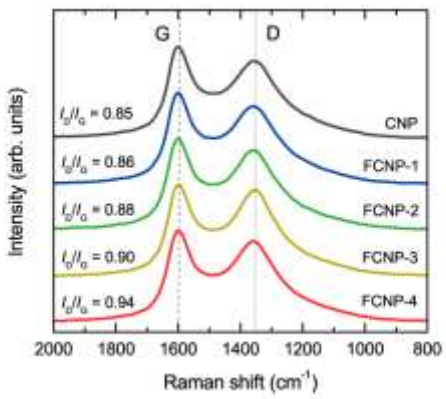

Fig. 4 Raman spectra with corresponding I_D/I_G ratios of CNP, FCNP-1, FCNP-2, FCNP-3, and FCNP-4 in the region of 800–2000 cm^{-1}. The vertical dashed and dotted lines are guides for the eyes to indicate the position of G- and D-bands, respectively.

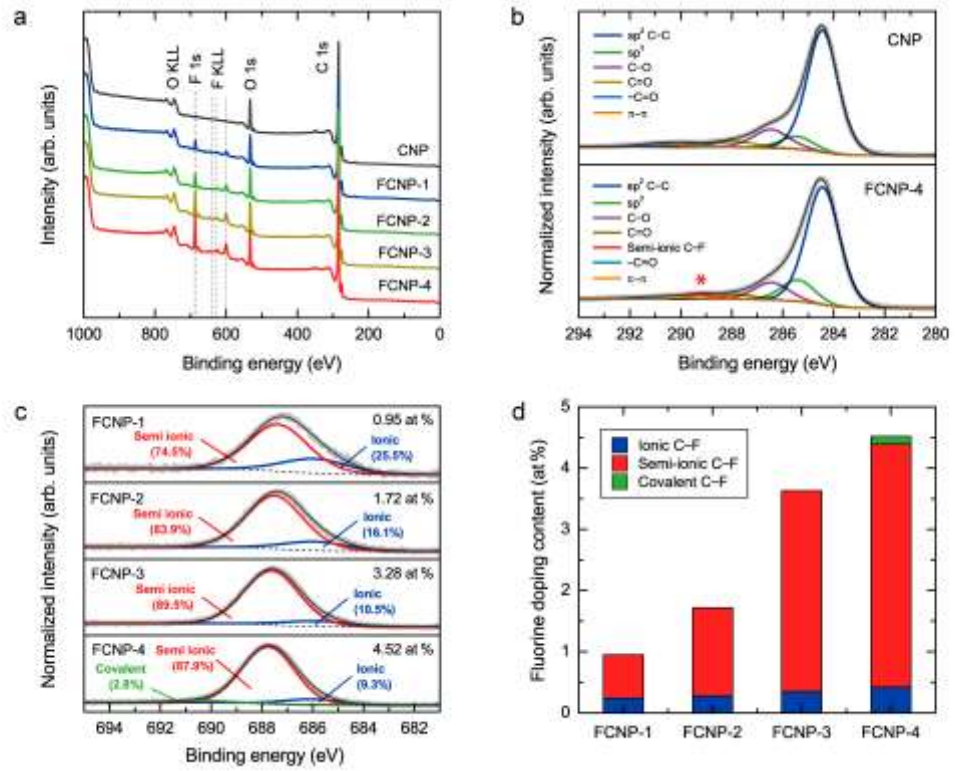

Fig. 5 (a) XPS survey spectra of CNP and FCNPs. The vertical dashed and dotted lines are guide for the eyes to indicate the position of F 1s and F KLL peaks, respectively. (b) Comparative high-resolution XPS C 1s spectra of CNP and FCNP-4. (c) High-resolution XPS F 1s spectra with deconvolution and peak assignments of FCNPs. (d) The fluorine doping content (at%) of FCNPs, including covalent C–F, semi-ionic C–F, and ionic C–F bonds.

composition and chemical bonding state of the elements on the carbon surfaces. The XPS survey spectra of FCNPs reveal the evident peaks corresponding to carbon, oxygen, and fluorine elements (Fig. 5a). No detectable signals are attributable to the tungsten element for all samples, confirming a negligible electrode erosion effect during the synthesis. It is clear that the intensity of F 1s peak becomes progressively higher in proportion to the amount of fluorotoluene in the mixed precursor. From the XPS quantitative analysis, the fluorine doping content is found to be 0.94, 1.72, 3.28, and 4.52 at% for FCNP-1, FCNP-2, FCNP-3, and FCNP-4, respectively. This is evidence that the fluorine doping content can be tuned by varying the amount of fluorotoluene in the mixed precursors. The SEM/EDS elemental mapping analysis of FCNPs shows the presence of fluorine atoms evenly distributed over the investigated large area (Fig. S1†), confirming the uniform incorporation of fluorine atoms in carbon particles. Figure 5b presents the comparison of high-resolution XPS C 1s spectra with peak deconvolution of CNP and FCNP-4. High-resolution XPS C 1s spectra of both CNP and FCNP-4 show the most pronounced peak centered at 284.5 ± 0.1 eV, corresponding to the sp^2 carbon bonding configuration. A long tail at higher binding energies is composed of several peaks assigning to sp^3 carbon (285.4 ± 0.2 eV), C–O (286.4 ± 0.2 eV), C=O (288.0 ± 0.1 eV), O–C=O (*e.g.* carbonyl and carboxylic: 289.7 ± 0.2 eV), and π–π interaction (290.8 ± 0.1 eV).[43] Importantly, an additional weak intensity peak at 289.2 eV (denoted as ∗) appears for FCNP-4, which confirms the presence of the semi-ionic C–F bonds.[21,44–46] It is also important to note the slight suppression of sp^2 peak intensity as the fluorine doping content increases (Fig. S2†). This result suggests that the incorporation of fluorine atoms causes the structural deformation or lowers the degree of sp^2 bonding of the carbon structure, which is consistent with the result from the Raman spectroscopy measurement. The presence of O 1s peak for all samples is likely due to the surface oxidation upon exposure to air (Fig. S3†). Figure 5c shows high-resolution XPS F 1s spectra of FCNPs with deconvolution and peak assignment. The XPS F 1s peaks of FCNP-1, FCNP-2, and FCNP-3 can be divided into two peaks centered at 685.9 ± 0.1 eV and 687.5 ± 0.2 eV, which can be assigned to ionic C–F and semi-ionic C–F bonds, respectively.[45–47] However, the XPS F 1s peak of FCNP-4 can be resolved into three peaks. In addition to ionic C–F and semi-ionic C–F bonds, the weak peak of covalent C–F bond is also observed at a higher binding energy of 690.0 eV.[46–48] This result indicates that the C–F bonds on FCNPs mainly exhibit a semi-ionic character. By increasing the overall fluorine doping content, the content of ionic C–F bond progressively increases (0.24–0.42 at%), while that of semi-ionic C–F clearly increases (0.71–3.97 at%), as shown in Fig. 5d. At a low fluorine doping content (FCNP-1), the relative percentage of ionic and semi-ionic C–F bonds is estimated to be 24.5% and 75.5%, respectively. However, with increasing fluorine doping content, the π electrons contributing to the C–F bonds become more localized, resulting in a change in C–F bond length and subsequently diminishing the ionic character. Therefore, most C–F bonds tend to be formed as semi-ionic type (83.9–87.9%) at higher fluorine doping contents. This finding indicates that the carbon particles generated in the presence of fluorine atoms and ions under solution plasma process would lead to the favorable formation of fluorine intercalation with ionic C–F and semi-ionic C–F bonds on FCNPs. Fluorine atoms bonded to carbon atoms with ionic and

semi-ionic types play the role of an electron acceptor, which thus facilitates charge transfer between fluorine and carbon, leading to higher conductivity as well as modifying the electronic properties of the pristine carbon.[49,50] However, the covalent fluorocarbons typically exhibit low electrical conductivity due to loss of graphitization.[51,52]

3.4 Electrocatalytic activity toward oxygen reduction reaction

The electrocatalytic activity for the ORR of all samples was first evaluated by cyclic voltammetry (CV) in 0.1 M KOH solution. The stable CV curves in 0.1 M KOH solutions saturated with N_2 and O_2 were recorded after 30 cycles in the potential range from –0.9 to 0.1 V at a scan rate of 50 mV s^{-1}. The featureless voltammetric current is observed for all samples in the N_2-saturated solution (Fig. S4†). In contrast, a single well-defined cathodic peak corresponding to the ORR can be observed for all samples in O_2-saturated solution (Fig. 6a and Fig. S4†). With increasing fluorine doping content, the ORR peak becomes more intense and shifts slightly toward a more positive potential, indicating improved ORR activity. To gain more insight into the electrocatalytic activity for the ORR, linear sweep voltammetry (LSV) measurements on an RDE were carried out in an O_2-saturated 0.1 M KOH solution at a scan rate of 10 mV s^{-1} and a rotation speed of 1600 rpm (Fig. 6b). The evolution of onset potential and limiting current density for the ORR obtained from the LSV curves show a similar changing trend with the CV curves. The LSV curve of CNP exhibits relatively poor ORR activity with an onset potential of –0.26 V and a low limiting current density of 1.8 mA cm^{-2} at –0.6 V. Upon increased fluorine doping content, the onset potential for the ORR progressively shifts to a more positive direction, and the limiting current density also increases. Among the samples studied, FCNP-4 shows the highest ORR activity in terms of both onset potential (–0.22 V) and limiting current density (2.76 mA cm^{-2} at –0.6 V). Such a gradual positive shift in onset potential and significant increase in limiting current density are evidence that the fluorine doping on the carbon materials has made a significant contribution to improving ORR activity in 0.1 M KOH solution. To elucidate further the ORR mechanisms on CNP and FCNPs, a series of LSV curves on an RDE were carried out at various rotation speeds from 225 to 2500 rpm in an O_2-saturated 0.1 M KOH solution with a scan rate of 10 mV s^{-1} (Fig. S5†). It is obvious that the diffusion-limiting current density continuously increases with an increase in the rotation speed owing to the shortened diffusion layer.[53] On the basis of the LSV measurements at various rotation speeds, the electron transfer number per O_2 molecule (n) in the ORR process can be determined from the Koutecky–Levich (K–L) equations as follows:[54]

$$\frac{1}{J} = \frac{1}{J_K} + \frac{1}{J_L} = \frac{1}{J_K} + \frac{1}{B\omega^{1/2}} \quad (1)$$

$$B = 0.62nFD_O^{2/3}v^{-1/6}C_O \quad (2)$$

where J is the measured current density, J_K is the kinetic-limiting current density, J_L is the diffusion-limiting current density, ω is the angular velocity of electrode ($\omega = 2\pi N$; N is the rotation speed in rpm), F is the Faraday constant (96485 C mol^{-1}), D_O is the diffusion coefficient of O_2 in the electrolyte (1.9×10^{-5} cm^2 s^{-1}),

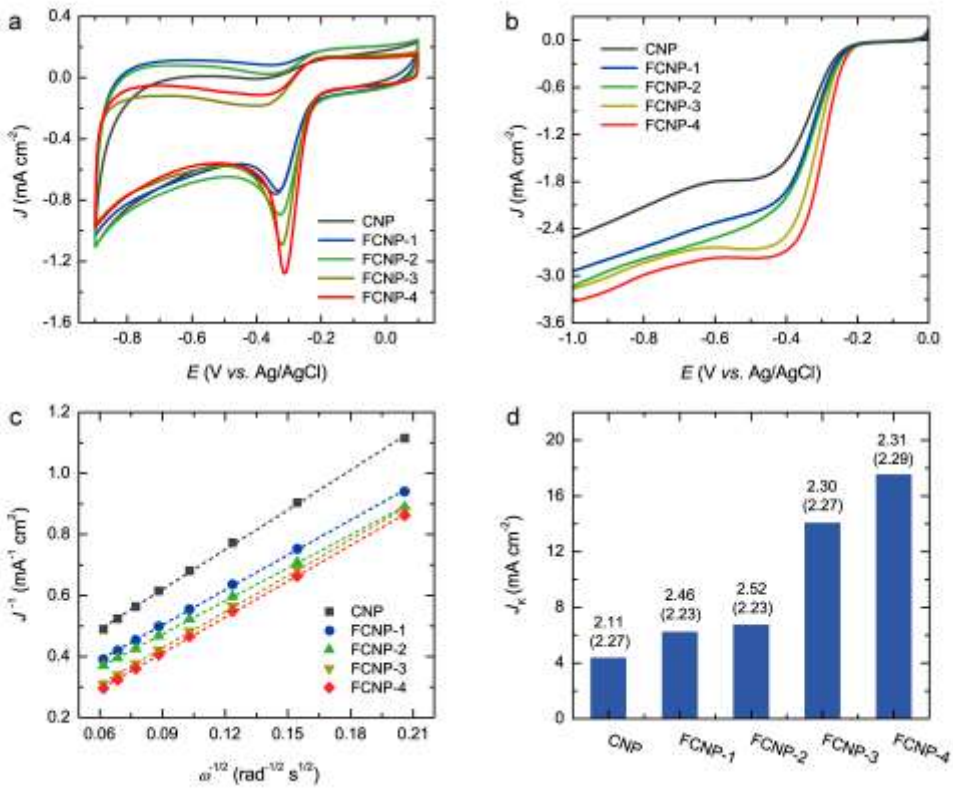

Fig. 6 Electrochemical measurements: (a) CV curves of CNP and FCNPs in an O_2-saturated 0.1 M KOH solution at a scan rate of 50 mV s^{-1}. (b) LSV curves of CNP and FCNPs in an O_2-saturated 0.1 M KOH solution at a scan rate of 10 mV s^{-1} and a rotation speed of 1600 rpm. (c) The K–L plots of J^{-1} *versus* $\omega^{-1/2}$ of CNP and FCNPs at a potential of –0.5 V derived from the LSV curves at rotation speed ranging from 225 to 2500 rpm. (d) Summary of J_K and n values derived from the K–L analysis and RRDE measurement (values in parentheses) of CNP and FCNPs at a potential of –0.5 V.

v is the kinematic viscosity of the electrolyte (0.01 cm^2 s^{-1}), and C_O is the bulk concentration of O_2 in the electrolyte (1.2×10^{-6} mol L^{-1}). The constant 0.62 is adopted when the rotation speed is expressed in radians per second (rad s^{-1}). The K–L plots of J^{-1} *versus* $\omega^{-1/2}$ of all samples show a good linearity in the investigated potentials ranging from –0.35 and –1.0 V (Fig. S6†). The parallel characteristics of linear fitting lines are observed in the potentials between –0.4 and –0.6 V, indicating a first-order ORR kinetic with respect to oxygen. The n values calculated from the slope of the K–L plots are in the range between 2.10 to 3.50 with no obvious change with increasing fluorine doping content over the potential range between −1.0 and −0.35 V (Fig. S7†). At a potential of –0.5 V, the n values are 2.11, 2.46, 2.52, 2.30, and 2.31 for CNP, FCNP-1, FCNP-2, FCNP-3, and FCNP-4, respectively. This result indicates that the mechanism of the ORR catalyzed on CNP and FCNPs mainly proceeds through a dominant two-electron transfer pathway that the first reduces to peroxide species (HO_2^-) as an intermediate and then further reduces to OH^-. Rotating-ring disk electrode (RRDE) measurements also were performed to confirm the n values derived from the K–L plots (Fig. S9†). The mechanism of the ORR process can be verified by monitoring the formation of intermediate peroxide species (*i.e.*, HO_2^- in the alkaline solution) on the basis of ring and disk currents (see ESI† for detailed calculations). As shown in Fig. S10a†, the HO_2^- yields are calculated to be about 75–90% for both CNP and FCNPs over the potential range from –0.35 to –1.0 V. The n values obtained from the RRDE measurement are quite consistent with those derived from the K–L analysis (Fig. 6d and Fig. S10b†).

Furthermore, the ORR activity can be quantitatively determined in term of J_K from the intercept of the linearly fitted K–L plot. The calculated J_K values with the corresponding n values obtained from the K–L plots and RRDE measurements at –0.5 V are comparatively shown in Fig. 6d. The J_K value is estimated to be 4.38 mA cm^{-2} for CNP, and significantly increases with increasing fluorine doping content (6.25–17.54 mA cm^{-2}) at –0.5 V. The increase in J_K with increasing fluorine doping content is also observed in the mixed kinetic-diffusion control region (Fig. S8†). The above results can allow the conclusion that the incorporation of fluorine atoms into the carbon structure can lead to the enhancement of ORR activity in terms of onset potential and limiting current density. However, it seems to have little influence on the modification of ORR mechanism in an alkaline solution.

The role of fluorine doping on the improvement of ORR activity can be explained by the combination of electrochemical data, XPS analyses, and specific surface areas. Carbon with high specific surface area is crucial for promoting ORR activity owing to more active catalytic sites and easy accessibility for electrolyte.[55,56] However, in our study, the ORR activity of FCNPs is enhanced at higher fluorine doping contents although the specific surface area decreases, thereby implying that the specific surface area may not play an essential role in the improved ORR activity. In association with the XPS analysis, the improved ORR activity of FCNPs is believed to be mainly attributed to the presence of ionic C–F and semi-ionic C–F bonds existed on the carbon surface. Sun *et al* proposed that the ORR activity order on FCNPs was found to be: ionic C–F > semi-ionic C–F > covalent C–F.[21,22] The calculation using density functional theory (DFT) revealed that the incorporation of fluorine atoms in the forms of ionic and semi-ionic states can induce more positive charge on the doped carbon, which results in the enhancement of interaction and adsorption between the O_2 molecule and carbon. The activity of π electrons on carbon also increases, leading to higher catalytic activity for the ORR and selectivity toward a four-electron pathway.[21,22] Unlike the previous reports, our results show that fluorine doping does not have a strong influence on modifying the ORR mechanism from a two to four-electron pathway. The unsatisfactory ORR activity of FCNPs may result from the small content of ionic C–F bond, low surface area, and low degree of graphitization compared to those of previous reports.[20,22,45] We anticipate that FCNPs with a higher content of ionic C–F bond, larger surface area, and higher degree of graphitization can lead to further improvement of ORR activity as well as selectivity toward a four-electron pathway. Beside these factors, the ratio of surface and bulk fluorine doping may be an important factor that influences the ORR mechanism. In our case, fluorine atoms are homogeneously doped both in the bulk and at the surface of carbon particles because of direct synthesis from an organic liquid compound. This is in contrast to previous reports that the fluorine atoms were doped only at the carbon surface through the post treatment process.[20–22,45] Therefore, we postulate that the bulk fluorine doping may result in the undesired electronic arrangement and consequently inhibit the ORR through a four-electron pathway.

The long-term durability and tolerance to the methanol oxidation of the ORR catalysts are other important requirements to realize practical applications of fuel cells. To confirm the durability, the current–time chronoamperometric response was performed on the most active FCNP-4 and a commercial 20% Pt/C at a constant potential of –0.5 V for 40000 s in O_2-saturated 0.1 M KOH (1600 rpm), as shown in Fig. 7a. The relative current density (J/J_0) of FCNP-4 exhibits a slow rate of attenuation with

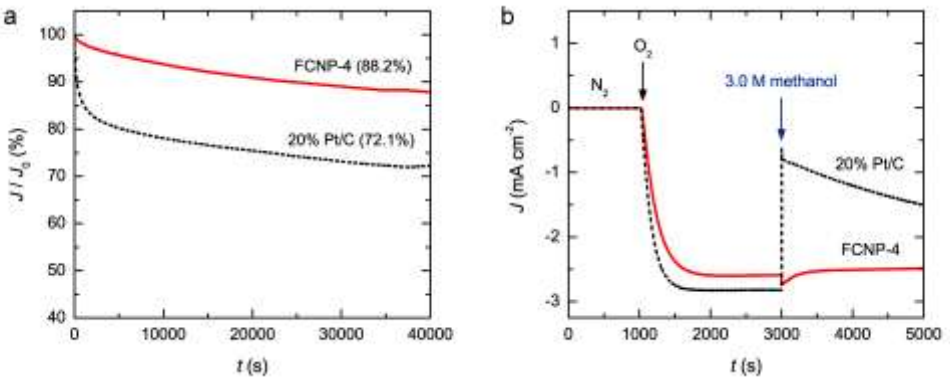

Fig. 7 (a) Current–time chronoamperometric response (1600 rpm) of FCNP-4 and 20% Pt/C at –0.5 V in an O_2-saturated 0.1 M KOH solution for 40000 s. (b) Methanol tolerance test of FCNP-4 and 20% Pt/C (1600 rpm) in an O_2-saturated 0.1 M KOH solution at –0.5 V and –0.3 V, respectively

retaining high current of approximately 88.2% after 40000 s. For the commercial 20% Pt/C, its relative current density decreases to approximately 72.1% after 40000 s. This result confirms that FCNP-4 has a superior long-term durability in an alkaline solution than that of 20% Pt/C. To evaluate tolerance to the methanol oxidation further, 3.0 M methanol was introduced into an O_2-saturated 0.1 M KOH solution during the measurement of current–time chronoamperometric response (Fig. 7b). After introduction of 3.0 M methanol, the ORR current density of FCNP is kept at almost the same level, while 20% Pt/C exhibit a large decrease in ORR current density. This result proves that the ORR activity of FCNP-4 exhibits stronger tolerance to methanol oxidation than that of 20% Pt/C.

4 Conclusions

The FCNPs with tunable fluorine doping content have been successfully synthesized *via* a one-step solution plasma process at relatively low temperature and atmospheric pressure. The structural analyses reveal that FCNPs mainly exhibit a disordered amorphous structure, and the incorporation of fluorine atoms into the carbon structure leads to the formation of more structural defect sites and lattice expansion. The electrocatalytic activity toward the ORR of FCNPs in alkaline solution can be significantly improved in terms of both onset potential and limiting current density with increasing fluorine doping content. However, their ORR activity tends to dominantly proceed dominantly through a two-electron pathway. Combined electrochemical and XPS data reveal that the presence of ionic C–F and semi-ionic C–F bonds existing on the carbon surface play essential roles in the improvement of ORR activity. The durability test shows that FCNPs have longer-term durability and stronger tolerance to methanol oxidation than those of a commercial 20% Pt/C. We believe that a positive correlation between the ORR activity and fluorine doping in this study will serve as a strong foundation for further development of FCNPs as ORR catalyst in fuel cell and related applications. In addition to the context of ORR, FCNPs may also be of interest for the electrochemical synthesis of hydrogen peroxide owing to their selective two-electron transfer pathway.

[a] *Department of Materials Science and Engineering, Faculty of Engineering, Shibaura Institute of Technology, Tokyo 135-8548, Japan E-mail: i036050@ sic.shibaura-it.ac.jp, ishizaki@sic.shibaura-it.ac.jp; Fax: +81-34-859-8101; Tel: +81-35-859-8115*
[b] *Department of Materials, Physics and Energy Engineering, Graduate School of Engineering, Nagoya University, Nagoya 646-8603, Japan*
[c] *Green Mobility Collaborative Research Center, Nagoya University, Nagoya 464-8603, Japan*
[d] *Core Research for Evolutional Science and Technology (CREST), Japan Science and Technology Agency (JST), Saitama 333-0012, Japan*

† Electronic Supplementary Information (ESI) available: SEM/EDS elemental mapping, high-resoltuion XPS C 1s and O 1s spectra of all samples, CV curves of all samples recored in N_2- and O_2-saturated 0.1 KOH solutions at 50 mV s^{-1}, a series of LSV curves of all samples at different rotation speeds, the K–L plots derived from LSV curves at different rotation speeds in the potential range from –1.0 to –0.4 V, electron transfer number determined from the K–L plots of all samples at various potentials, J_K of all samples in the mixed kinetic-diffusion control region, disk and ring current measured on RRDE for all samples (1600 rpm), electron transfer number and HO_2^- yield calculated from disk and ring currents at different potentials. See DOI: 10.1039/b000000x/

Notes and references

1 J. P. Paraknowitsch and A. Thomas, *Energy Environ. Sci*., 2013, **6**, 2839.
2 N. Daems, X. Zheng, I. F. J. Vankelecom and P. P. Pescarmona, *J. Mater. Chem. A*, 2014, **2**, 4085.
3 D. W. Wang and D. Su, *Energy Environ. Sci.*, 2014, **7**, 576.
4 L. Zhang and Z. Xia, *J. Phys. Chem. C*, 2011, **115**, 11170.
5 J. Liang, Y. Jiao, M. Jaroniec and S. Z. Qiao, *Angew. Chem. Int. Ed.*, 2012, **51**, 11496.
6 I. Y. Jeon, S. Zheng, L. Zhang, H. J. Choi, J. M. Seo, Z. Xia, L. Dai and J. B. Baek, *Adv. Mater*., 2013, **25**, 6138.
7 Z. Lin, M. K. Song, Y. Ding, Y. Liu, M. Liu and C. P. Wong, *Phys. Chem. Chem. Phys.*, 2012, **14**, 3381.
8 W. J. Lee, U. N. Maiti, J. M. Lee, J. Lim, T. H. Han and S. O. Kim, *Chem. Commun*., 2014, **50**, 6818.
9 Yang, J. Liu, R. Zhou, Z. Chen, H. Xu, S. Z. Qiao and M. J. Monteiro, *J. Mater. Chem. A*, 2014, **2**, 18139.
10 L. Yang, S. Jiang, Y. Zhao, L. Zhu, S. Chen, X. Wang, Q. Wu, J. Ma, Y. Ma and Z. Hu, *Angew, Chem. Int. Ed.*, 2011, **50**, 7132.
11 Z. H. Sheng, H. L. Gao, W. J. Bao, F. B. Wang and X. H. Xia, *J. Mater. Chem*., 2012, **22**, 390.
12 Z. W. Liu, F. Peng, H. J. Wang, H. Yu, W. X. Zheng and J. Yang, *Angew. Chem. Int. Ed*., 2011, **50**, 3257.
13 J. Wu, Z. Yang, X. Li, Q. Sun, C. Jin, P. Strasser and R. Yang, *J. Mater. Chem. A*, 2013, **1**, 9889.
14 J. E. Park, Y. J. Jang, Y. J. Kim, M. S. Song, S. Yoon, D. H. Kim and S.-J. Kim, *Phys. Chem. Chem. Phys*., 2014, **16**, 103.
15 Z. Yang, Z. Yao, G. Li, G. Fang, H. Nie, Z. Liu, X. Zhou, X. Chen and S. Huang, *ACS Nano*, 2012, **6**, 205.
16 A. A. Wohlgemuth, R. J. White, M. G. Willinger, M. M. Titrici and M. Antonietti, *Green Chem*., 2012, **14**, 1515.
17 C. H. Choi, S. H. Park and S. I. Woo, *J. Mater. Chem*., 2012, **22**, 12107.
18 C. H. Choi, S. H. Park and S. I. Woo, *ACS Nano*, 2012, **6**, 7084.
19 Y. Zhao, L. Yang, S. Chen, X. Wang, Y. Ma, Q. Wu, Y. Jiang, W. Qian and Z. Hu, *J. Am. Chem. Soc*., 2013, **135**, 1201.
20 X. Sun, Y. Zhang, P. Song, J. Pan, L. Zhuang, W. X and W. Xing, *ACS Catal*., 2013, **3**, 1726.
21 X. Sun, P. Song, T. Chen, J. Liu and W. Xu, *Chem. Commun*., 2013, **49**, 10296.
22 X. Sun, P. Song, Y. Zhang, C. Liu, W. Xu and W. Xing, *Sci. Rep*., 2013, **3**, 2505.
23 X. Wang, G. Sun, P. Routh, D. H. Kim, W. Huang and P. Chen, *Chem. Soc. Rev*., 2014, **43**, 7067.
24 H. Shi, Y. Shen, F. He, Y. Li, A. Liu, S. Liu and Y. Zhang, *J. Mater. Chem. A*, 2014, **2**, 15704.
25 C. N. R. Rao, K. Gopalakrishnan and A. Govindaraj, *Nanotoday*, 2014, **9**, 324.
26 L. Feng, Y. Chen and L. Chen, *ACS Nano*, 2011, **5**, 9611.
27 Y. Zhang, K. Fugane, T. Mori, L. Niu and J. Ye, *J. Mater. Chem*., 2012, **22**, 6575.
28 J. Senthilnathan, K. S. Rao and M. Yoshimura, *J. Mater. Chem. A*, 2014, **2**, 3332.
29 J. Chen, X. Wang, X. Cui, G. Yang and W. Zheng, *Catal. Commun*., 2014, **46**, 161.
30 J. Z. Du, S. Wang, C. Kong, Q. Deng, G. Wang, C. Laing and H. Tang, *J. Sold State Electrochem*., 2015, DOI 10.1007/s10008-015-2773-3.
31 D. Wei, L. Peng, M. Li, H. Mao, T. Niu, C. Han, W. Chen and A. T. S. Wee, *ACS Nano*, 2015, **9**, 164.
32 N. A. Kumar, H. Nolan, N. McEvoy, E. rezvani, R. L. Doyle, M. E. G. Lyons and G. S. Duesberg, *J. Mater. Chem. A*, 2013, **1**, 4431.
33 G. Panomsuwan, S. Chiba, Y. Kaneko, N. Saito and T. Ishizaki, *J. Mater. Chem. A*, 2014, **2**, 18677.
34 G. Panomsuwan, N. Saito and T. Ishizaki, *Phys. Chem. Chem. Phys*., 2015, **17**, 6227.
35 T. Ishizaki, S. Chiba, Y. Kaneko and G. Panomsuwan, *J. Mater. Chem. A*, 2014, **2**, 10589.
36 D. W. Kim, O. L. Li and N. Saito, *Phys. Chem. Chem. Phys*., 2015, **17**, 407.
37 L. Kumari and S. V. Subramanyam, *Mater. Res. Bull*., 2006, **41**, 2000.

38 V. Sahu, S. Shekhar, P. Ahuja, G. Gupta, S. K. Singh, A. K. Sharma and G. Singh, *RSC Adv*., 2013, **3**, 3917.
39 A. Ōya and H. Marsh, *J. Mater. Sci*., 1982, **17**, 309.
40 N. Tsubouchi, C. Xu and Y. Ohtsuka, *Energy Fuel*, 2003, **17**, 1119.
41 A. C. Ferrari and J. Robertson, *Phys. Rev. B*, 2000, **61**, 14095.
42 A. C. Ferrari and J. Robertson, *Phys. Rev. B*, 2001, **64**, 075414.
43 A. V. Palenzuela, L. Zhang, L. Wang, P. L. Cabot, E. Brillas, K. Tsay and J. Zhang, *J. Phys. Chem. C*, 2011, **115**, 12929.
44 B. Shen, J. Chen, X. Yan and Q. Xue, *RSC Adv*., 2012, **2**, 6761.
45 H. Wang and A. Kong, *Mater. Lett*., 2014, **136**, 384.
46 T. Nakajima, M. Koh, V. Gupta and K. Lutar, *Electrochim. Acta*, 2000, **45**, 1655.
47 P. F. Fulvio, S. S. Brown, J. Adcock, R. T. Mayes, B. Guo, Z. G. Sun, S. M. Mahurin, G. M. Veith and S. Dai, *Chem. Mater*., 2011, **23**, 4420.
48 C. Sun, Y. Feng, Y. Li, C. Qin, Q. Zhang and W. Feng, *Nanoscale*, 2014, **6**, 2634.
49 A. K. Geim , K. S. Novoselov, *Nat. Mater.*, 2006, **6**, 183.
50 J. H. Lee, G. K. W. Koon, D. W. Shin, V. E. Federov, J. Y. Choi, J. B. Yoo and B. Özyilmaz, *Adv. Func. Mater*., 2013, **23**, 3329.
51 N. Watanabe, T. Nakajima and H. Touhara, Graphite Florides, Elsevier, Amsterdam, 1988, ch. 7.
52 W. H. Lee, J. W. Suk, H. Chou, Y. Hao, Y. Wu, R. Piner, D. Akinwande, K. S. Ki and R. S. Ruoff, *Nano Lett*., 2012, **12**, 2374.
53 W. Yang, T. P. Fellinger and M. Antonietti, *J. Am. Chem. Soc*., 2011, **138**, 206.
54 S. Treimer, A. Tang and D. C. Johnson, *Electroanal*., 2002, **14**, 165.
55 H. W. Liang, W. Wei, Z. S. Wu, X. Fen and K. Müllen, *J. Am. Chem. Soc*., 2013, **135**, 16002.
56 C. T. Hung, N. Yu, C. T. Chen, P. H. Wu, X. Han, Y. S. Kao, T. C. Liu, Y. Chu, F. Deng, A. Zheng and S. B. Liu, *J. Mater. Chem. A*, 2014, **2**, 20030.

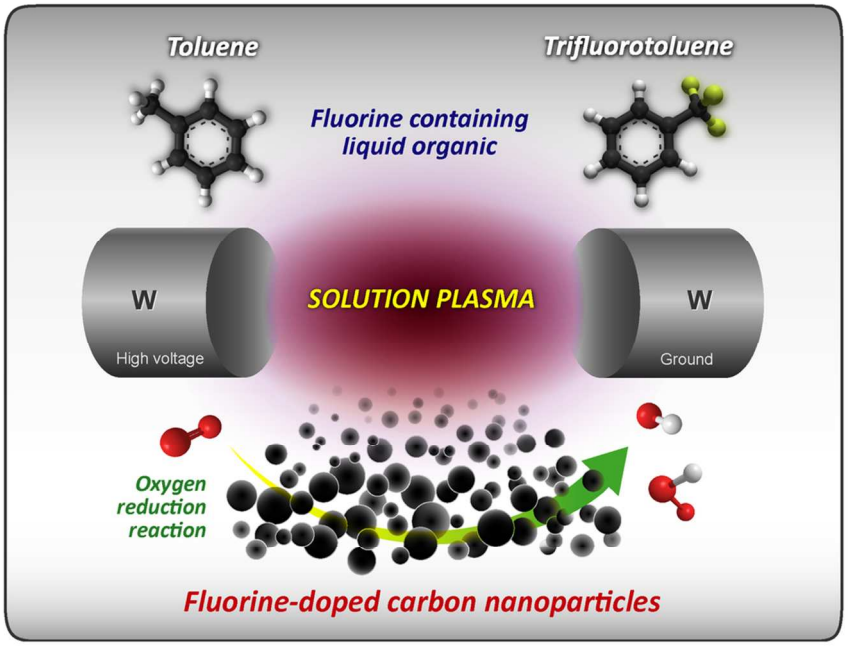

Fluorine-doped carbon nanoparticles were successfully synthesized via a simple one-step solution plasma process at room temperature and atmospheric pressure without the addition of metal catalyst.
50x41mm (600 x 600 DPI)